Exp Fluids
DOI 10.1007/s00348-007-0457-1

LETTER

A color-coded backlighted defocusing digital particle image velocimetry system

Wei-Hsin Tien · Patrick Kartes · Toru Yamasaki · Dana Dabiri

Received: 6 February 2007 / Revised: 5 December 2007 / Accepted: 13 December 2007
© Springer-Verlag 2008

Abstract Defocusing digital particle image velocimetry (DDPIV), as a true three-dimensional (3D) measurement technique, allows for the measurement of 3D velocities within a volume. Initially designed using a single CCD and 3-pinhole mask (Willert and Gharib in Exp Fluids 12:353–358, 1992), it has evolved into a multi-camera system in order to overcome the limitations of image saturation due to multiple exposures of each particle. In order to still use a single camera and overcome this limitation, we have modified the original single CCD implementation by placing different color filters over each pinhole, thus color-coding each pinhole exposure, and using a 3-CCD color camera for image acquisition. Due to the pinhole mask, there exists the problem of a significant lack of illumination in a conventional lighting setup, which we have solved by backlighting the field-of-view and seeding the flow with black particles. This produces images with a white background superimposed with colored triple exposures of each particle. A color space linear transformation is used to allow for accurate identification of each pinhole exposure when the color filters' spectrum does not match those of the 3-CCD color camera. Because the imaging is performed with a multi-element lens instead of a single-element lens, an effective pinhole separation, d_e, is defined when using a pinhole mask within a multi-element lens. Calibration results of the system with and without fluid are performed and compared, and a correction of the effective pinhole separation, d_e, due to refraction through multiple surfaces is proposed. Uncertainty analyses are also performed, and the technique is successfully applied to a buoyancy-driven flow, where a 3D velocity field is extracted.

W.-H. Tien · P. Kartes · D. Dabiri (✉)
Department of Aeronautics and Astronautics,
University of Washington, Seattle, WA 98195, USA
e-mail: dabiri@aa.washington.edu

T. Yamasaki
Software Cradle Co., Ltd., 6-1-1, Nishinakajima,
Yodogawa-ku, Osaka 532-0011, Japan

1 Introduction

PIV has become a widely used quantitative flow visualization technique in today's fluid mechanics research due to its ability to provide non-intrusive, highly resolved measurement of planar velocity fields. With the use of ever-advancing CCD cameras, digital data acquisition systems, and sophisticated algorithms, DPIV continues to evolve and flourish. One of the key advancements is the development of defocusing digital particle image velocimetry (DDPIV), which allows for 3D velocity measurements within a volume. First proposed and established by Willert and Gharib (1992), this technique uses the defocusing concept to obtain a particle's position in three dimensions. Using a three lens/CCD setup and a cross-correlation algorithm on sequential images, Pereira et al. (2000) mapped the bubbly flow field about a propeller using this concept. An error analysis with an uncertainty test was also reported. A 2D theoretical basis of the optical design and velocity estimation methodology, together with a multi-surface refraction correction scheme is later reported in Pereira et al. (2002). Kajitani and Dabiri (2005) established a full 3D characterization of the DDPIV system and its associated geometric uncertainty. Yoon and Kim (2006) adapted the defocusing concept and applied it to a micro-scale channel flow over a backward-facing step and obtained a time-averaged flow field. Since their

microscope's lens had multiple elements, they could not directly use the DDPIV relations established by Kajitani and Dabiri (2005), which were based on a single-element lens. They therefore developed a calibration-based method to determine the depth location. Pereira et al. (2007) proposed a calibration procedure to approximate the multi-element lens optical system to a single-element lens system model, thereby overcoming the difficulty of determining the depth location. They then applied the single-lens concept to image a micro-volume flow of an evaporating water droplet.

Initial implementations of DDPIV require three separate, yet properly coordinated, imaging systems integrated as a single unit to overcome the identification problem of overlapping particle exposures. This configuration is designed to image a large volume of interest because separating the three pinhole apertures into three individual lens/CCD systems makes it possible to increase the pinhole separation without using a costly customized large lens. Using this three-camera DDPIV system to measure velocities within small-scale flow fields has two major difficulties. First, due to its size and complexity, this type of system is hard to setup and calibrate. Second, with the presence of the pinhole mask, a high intensity light source is required to adequately illuminate the flow, which can noticeably heat and evaporate the fluid, thereby affecting the nature of the interrogated flow.

Efforts to avoid such difficulties in measuring flows within small volumes eventually lead to the original single camera configuration proposed by Willert and Gharib (1992), which has recently been used by Yoon and Kim (2006), and Pereira et al. (2007). Nevertheless, the main difficulties of this single camera configuration, the identification of overlapping triplets and the necessity of a high intensity illumination source, still remain. In addition, the compactness of microscope optical systems prevents the pinhole separation from being large. The purpose of this paper is to therefore, provide a solution that overcomes these two difficulties, and characterize this new system through calibration procedures and uncertainty analyses. Furthermore, a new calibration procedure is proposed, which allows for the multi-element single lens to be accurately modeled as a single-element single lens. Towards this end, Sect. 2 presents the modifications to the single-lens camera configuration and illumination system; Sect. 3 presents the color transformation algorithm that allows for accurate identification and separation of particle images within triplets; Sect. 4 presents the experimental setup used for calibration and experimentation; Sect. 5 presents the calibration method; Sect. 6 presents the uncertainty analyses; Sect. 7 presents an application to fluid flow; and finally Sect. 8 presents the conclusions.

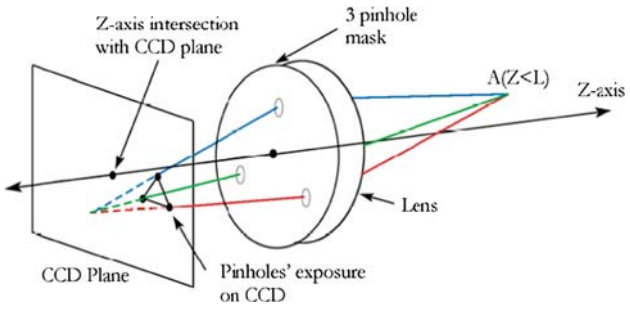

Fig. 1 The single lens DDPIV system concept (Pereira et al. 2000; Kajitani and Dabiri 2005)

2 Modified single lens 3DDPPIV system

The concept of the single camera DDPIV system is best described by a 3D representation of the imaging system in Fig. 1 (Pereira et al. 2000; Kajitani and Dabiri 2005). The light, reflecting from particles between the plane of focus and the lens plane (the defocused region), passes through the pinholes and forms triple exposures (triplets) on the CCD plane. The size of the triplets depends on the location of the particle within the defocused region. The original concept proposed by Willert and Gharib (1992) is difficult to use when the imaged particle density becomes sufficiently large due to overlapped triplet exposures, since they are difficult to identify, separate, and use towards particle identification. Furthermore, the necessity of the pinholes has the unfortunate consequence of severely reducing the amount of light that exposes the CCD.

The method we propose here makes two important modifications. First, a different color filter (red, green and blue) is overlaid onto each of the pinhole apertures, as shown in Fig. 2. Since the color-coded pinholes will result in colored images, a 3-CCD color camera is used for image acquisition. With this modification, the projected triplet image on the CCD plane is such that each pinhole's image will have a unique color, thus allowing for its identification.

Fig. 2 The *three color-filtered* pinholes on the aperture mask

Furthermore, if the pinhole exposures overlap, the resulting color is also unique, still allowing for identification of each of the overlapped particles. In this manner, it is now possible to image high particle densities while eliminating the need for the more complex three-camera/lens system. Details of how this is achieved are given in Sect. 3.

Second, the seeding and illumination methods of the test section are modified. In the previous DDPIV configuration, light illuminates each seeding particle and the CCD camera images the light reflected from the particles. Since the DDPIV system is imaging a volume, significantly more light is needed compared to planar PIV systems. The presence of the pinhole apertures further limits the amount of light reaching the CCD camera. Usually a laser system is needed to provide sufficient reflected light. In the present work, we propose a similar method used by Estevadeordal and Goss (2005) to overcome this difficulty. Initially, the test section is seeded with black, non-reflective particles. The aforementioned color filters over each pinhole preclude the use of a single wavelength laser illumination source, thereby necessitating the use of a white light source. This light source is set to intentionally illuminate towards the camera (forward scattering setup), resulting in an image with a white background and different colored triplet images. Figure 3a shows the resulting triplet if no color filters are used; Fig. 3b shows the resulting triplet if red, green, and blue color filters are used. The formation of the cyan, yellow and magenta triplet colors is addressed below.

Figure 4 shows how the defocused particle image (triplet) on the CCD plane is superimposed from the three pinhole apertures. Since black particles are imaged, these particles will block the light and form particle shadows on the images emerging from each of the red, green and blue filtered pinhole apertures. When the red and the green planes are superimposed, the image will result in a yellow background (red + green), but with green/red particle images where the black particle has blocked light in the red/green planes, respectively. Similarly, the other two combinations of the color planes (green + blue, red + blue) also form the cyan and magenta regions, respectively, with blue/green particle images and blue/red particle images, respectively (see Fig. 4). Finally, when all three planes are superimposed as shown in the central region of the

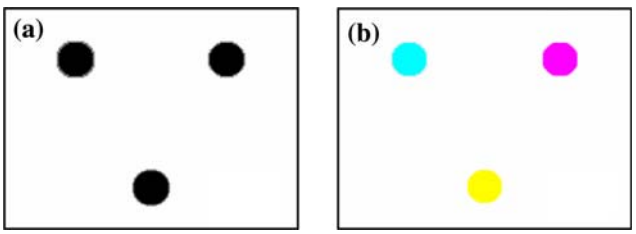

Fig. 3 The *triplet image* formed on a 3-CCD color camera: **a** without color filters, **b** with color filters

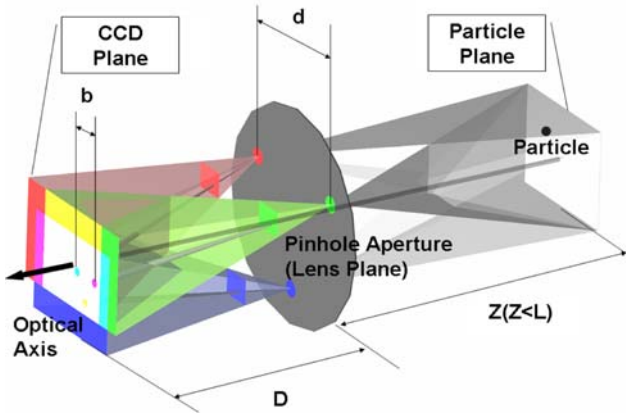

Fig. 4 Defocused images obtained from a black particle illuminated with backlighting from a white light source through three color filters. Also seen are the superimposed images from each of the two color plane overlays and the superposition of the three color planes

CCD plane, the image will result in a white (red + green + blue) background, but with cyan (green + blue)/yellow (red + green)/magenta (blue + red) particle images. This modification also provides good contrast between the background and the particle images, which is useful for particle identification.

3 Identification of defocused particles by color separation

To identify the color-coded triplet images described above, a method for separating the three colors is necessary. In theory, this can be easily done if the spectrums of each of the red, green, and blue color filters perfectly match the spectrum of each of the red, green, and blue CCDs, respectively, since light emerging from each of the color filtered pinholes would expose only their respective CCDs. In reality, the spectrum of the color filters and the CCDs do not match, thereby causing multiple pinhole exposures on each of the CCDs. A transformation algorithm defined by Pratt (1991) is therefore adopted to correct this problem.

The main concept of the transformation algorithm is to transform colors defined within an original set of primaries, $[P_1]$, $[P_2]$, and $[P_3]$, into another color space defined by a new set of primary colors $[P'_1]$, $[P'_2]$ and $[P'_3]$. With this new set of primary colors, an arbitrary color, C, can be expressed by a new set of tristimulus values, $\boldsymbol{T}'(C)$, that are based on the new set of primaries,

$$\boldsymbol{T}'(C) = \begin{bmatrix} T'_1(C) \\ T'_2(C) \\ T'_3(C) \end{bmatrix}, \tag{1}$$

while the arbitrary color can also be expressed by the tristimulus values defined with the original primaries, $\boldsymbol{T}(C)$,

$$\boldsymbol{T}(C) = \begin{bmatrix} T_1(C) \\ T_2(C) \\ T_3(C) \end{bmatrix}. \tag{2}$$

Using the linear transformation of the primary colors' tristimulus values derived by Pratt (1991), the color matched by the original set of primaries (Red/Green/Blue or *RGB*), $\boldsymbol{T}(C)$, can be transformed into the new set of primaries (Cyan/Magenta/Yellow or *CMY*), $\boldsymbol{T}'(C)$, by the following equation:

$$\begin{bmatrix} \mathrm{T}'_1(C) \\ \mathrm{T}'_2(C) \\ \mathrm{T}'_3(C) \end{bmatrix} = \begin{bmatrix} \begin{vmatrix} \mathrm{T}_1(C) & \mathrm{T}_1(P'_2) & \mathrm{T}_1(P'_3) \\ \mathrm{T}_2(C) & \mathrm{T}_2(P'_2) & \mathrm{T}_2(P'_3) \\ \mathrm{T}_3(C) & \mathrm{T}_3(P'_2) & \mathrm{T}_3(P'_3) \end{vmatrix} \Big/ \begin{vmatrix} \mathrm{T}_1(W) & \mathrm{T}_1(P'_2) & \mathrm{T}_1(P'_3) \\ \mathrm{T}_2(W) & \mathrm{T}_2(P'_2) & \mathrm{T}_2(P'_3) \\ \mathrm{T}_3(W) & \mathrm{T}_3(P'_2) & \mathrm{T}_3(P'_3) \end{vmatrix} \\ \begin{vmatrix} \mathrm{T}_1(P'_1) & \mathrm{T}_1(C) & \mathrm{T}_1(P'_3) \\ \mathrm{T}_2(P'_1) & \mathrm{T}_2(C) & \mathrm{T}_2(P'_3) \\ \mathrm{T}_3(P'_1) & \mathrm{T}_3(C) & \mathrm{T}_3(P'_3) \end{vmatrix} \Big/ \begin{vmatrix} \mathrm{T}_1(P'_1) & \mathrm{T}_1(W) & \mathrm{T}_1(P'_3) \\ \mathrm{T}_2(P'_1) & \mathrm{T}_2(W) & \mathrm{T}_2(P'_3) \\ \mathrm{T}_3(P'_1) & \mathrm{T}_3(W) & \mathrm{T}_3(P'_3) \end{vmatrix} \\ \begin{vmatrix} \mathrm{T}_1(P'_1) & \mathrm{T}_1(P'_2) & \mathrm{T}_1(C) \\ \mathrm{T}_2(P'_1) & \mathrm{T}_2(P'_2) & \mathrm{T}_2(C) \\ \mathrm{T}_3(P'_1) & \mathrm{T}_3(P'_2) & \mathrm{T}_3(C) \end{vmatrix} \Big/ \begin{vmatrix} \mathrm{T}_1(P'_1) & \mathrm{T}_1(P'_2) & \mathrm{T}_1(W) \\ \mathrm{T}_2(P'_1) & \mathrm{T}_2(P'_2) & \mathrm{T}_2(W) \\ \mathrm{T}_3(P'_1) & \mathrm{T}_3(P'_2) & \mathrm{T}_3(W) \end{vmatrix} \end{bmatrix}. \tag{3}$$

where *W* represents the reference white color.

To find the new set of primaries, a black dot patterned transparency is put within the defocusing region, thereby generating triplets with cyan, magenta, and yellow dots, and imaged with the modified DDPIV camera system. To identify cyan, magenta, and yellow in terms of the original *RGB* primaries, the background is separated from the particles by using its low saturation as a thresholding criterion. For the remaining pixels, the *RGB* color space is converted into the *HSV* color space in Matlab. The *HSV* color space describes color by three components: the Hue (in degrees), which describes the essence of the color (i.e., whether the color is blue or green), Saturation, which describes how much white is mixed with a particular hue (i.e., whether a color is red or pink), and Value, which describes how bright a color is (i.e., dark red vs. bright red). Figure 5 shows a typical distribution of the hue after its conversion to degrees, where its *CMY* peaks, (185.23, 297.48, 50.52), are slightly different than the standard *CMY* values, (180, 300, 60). It should be noted that this slight difference necessitates this procedure and precludes the use of the standard *RGB*-to-*CMY* transformation. Once the *CMY* peaks are identified, they are re-transformed to the *RGB* domain, so that they can be used within Eq. (3) to identify colors defined by the new *CMY* primaries for all pixels within the image that do not have low saturation values.

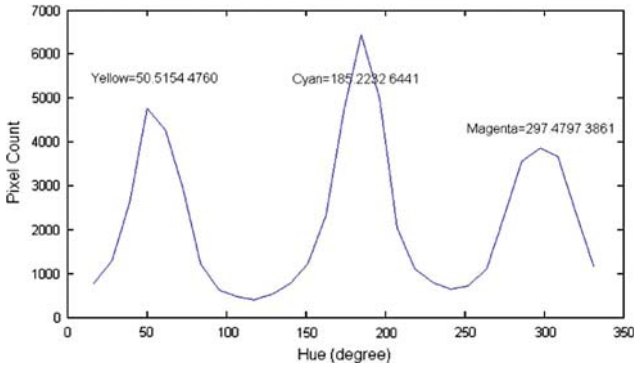

Fig. 5 Typical color-filtered pinhole hue histogram of a DDPIV image

Application of this procedure easily allows for splitting the three *CMY* channels, where each channel represents the intensity image from each pinhole. Figure 6 is a comparison of the original image containing a triplet of a defocused particle, its inversed intensity and the successfully separated pinhole images after the application of the color separation described above. The result of overlapped triplets from different defocused particles is shown in Fig. 7. While its intensity clearly cannot provide useful information to identify each exposure, the color separation procedure clearly identifies overlapped particles.

4 Experimental setup

Figure 8 shows the experimental setup of the system used for calibration as well as for actual experiments. This system consists of a Xenon flash lamp, (Perkin Elmer FX-4400) a Nikon AF Micro 105 mm camera lens, a pinhole mask with 2.74 mm diameter pinholes that are located at the vertices of an equilateral triangle with side lengths of 15 mm, Roscolux color filters (CalColor 90 Red #4690, CalColor 90 Green 4490 and Calcolor 90 Blue #4290), a 640 × 480 pixels Sony XC-007 3-CCD chip camera, and a translation stage. The three-pinhole mask with color filters is placed inside the lens. The lens is attached to the camera via a bellows tube at a distance such that the measured magnification factor is 2.69. The resulting imaging volume is $3.35 \times 2.5 \times 1.5\ \mathrm{mm}^3$. The light source is pulsed at 15 Hz and located sufficiently far from the lens so the resulting white background is uniform. Twenty micrometer diameter polystyrene particles manufactured by Polysciences Inc. are dyed black to absorb incident light, and are used to seed the flow within the test section.

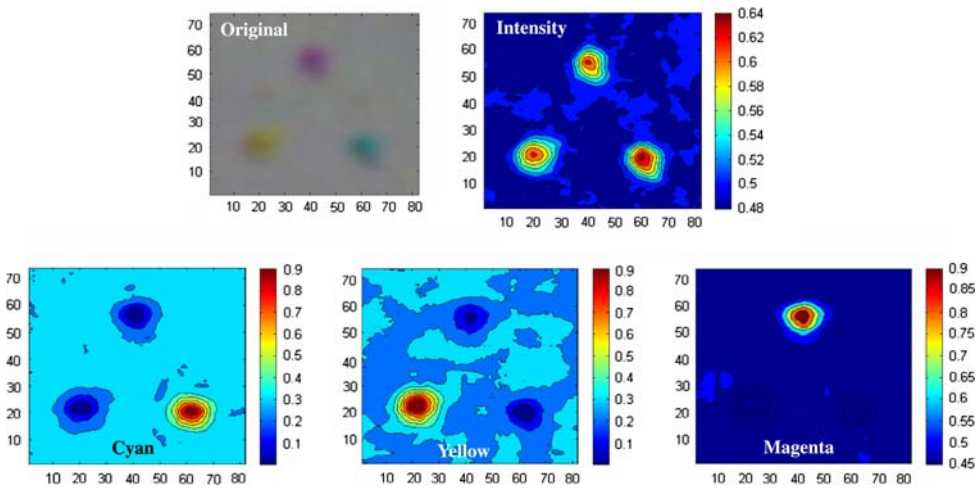

Fig. 6 Identification and separation of particle exposures within a single triplet using the color separation algorithm

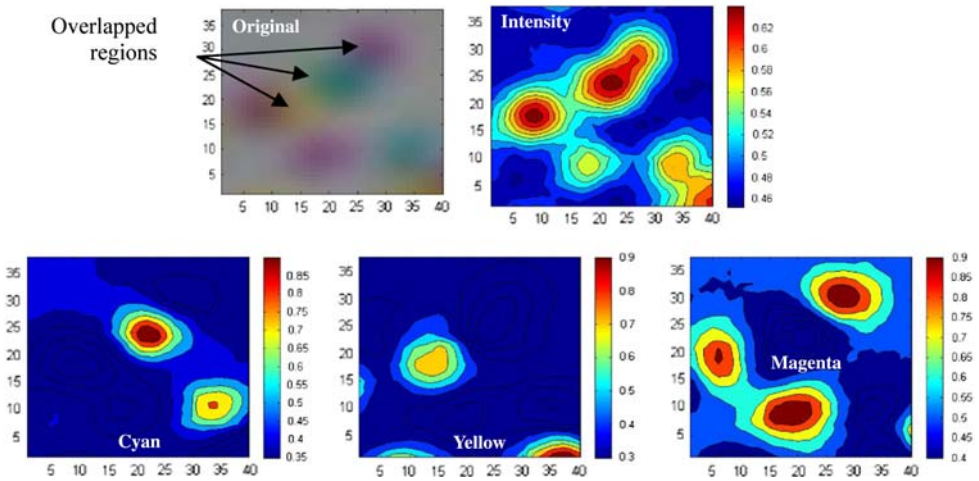

Fig. 7 Identification and separation of particle exposures within overlapped triplets using the color separation algorithm

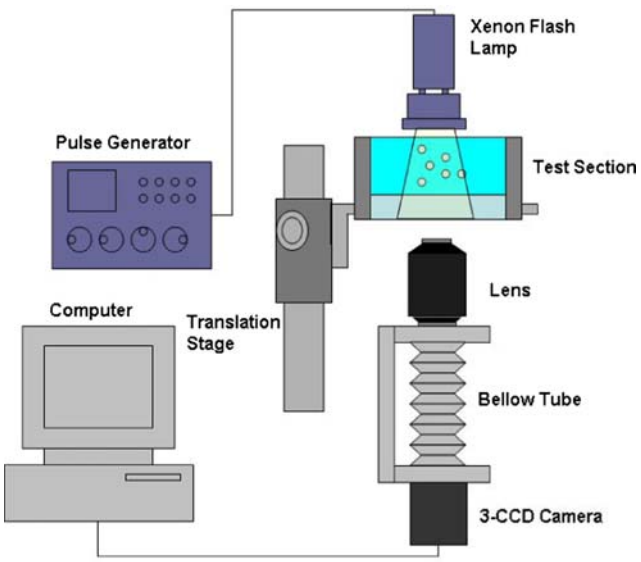

Fig. 8 Experimental setup

5 Calibration of the particle spatial coordinates

5.1 Concept and characteristic equations

The 3D mapping relation between the spatial coordinates (X, Y, Z) and image coordinates (x, y) of each pinhole exposure image has been derived previously (Kajitani and Dabiri 2005). The spatial coordinates, X and Y, are functions of the average image coordinates, x_0 and y_0, magnification of the optical system, M, distance from the lens plane to the reference plane, L, and spatial coordinate, Z

$$X = \frac{-x_0 Z}{ML}, \quad Y = \frac{-y_0 Z}{ML}. \tag{4}$$

The spatial coordinate, Z, is also shown to be

$$Z = \left(\frac{1}{L} + \frac{b}{MdL}\right)^{-1}, \tag{5}$$

where b is the image separation and d is the distance between the pinhole apertures, as shown in Fig. 9.

Since these derivations assumed that the system was comprised of a single-element lens, d has been a known parameter. However, since the present lens contains multiple elements, and since the pinhole mask is placed within the lens, an "effective" pinhole separation, d_e, should be used rather than the actual pinhole separation, d, in the above equations. This inconsistency is a source of error in the displacement measurements and will also reduce the precision of the velocity measurements. In addition, since the lens is multi-element, L is not readily known either. To solve these problems, a calibration procedure is developed to determine the "effective" pinhole separation, d_e, as well as compensate for the unknown distance, L.

Particles placed on the bottom surface of the test section are first imaged at the focal plane, resulting in only single particle exposures. The test section is then moved towards the lens system by a distance h_1 (shown in Fig. 9), causing defocused triple particle exposures with a separation distance b_1. The Z location of a particle on the bottom surface of the test section is then calculated using Eq. (5), where d is replaced by the "effective" pinhole separation d_e:

$$Z = \left(\frac{1}{L} + \frac{b}{Md_eL}\right)^{-1}. \tag{6}$$

Using the approach taken by Pereira et al. (2007), Z can be represented by the displacement h_1 and L

$$L - Z = h_1 \Rightarrow Z = L - h_1, \tag{7}$$

where L can be determined by the nominal magnification M and focal length of the lens f from the lens equation:

$$M = \frac{f}{L-f} \Rightarrow L = \frac{f(1+M)}{M}. \tag{8}$$

Combining Eqs. (6)–(8), the effective spacing of the pinhole apertures, d_e, can be calculated from the image separation b_1, magnification M, focal length of the camera f, and the displacement h_1:

$$d_e = \frac{b_1}{M}\left(\frac{f(1+M)}{Mh_1} - 1\right). \tag{9}$$

Rewriting Eq. (9), and assuming $f \gg h_1$, the relation of b_1 and h_1 can be written as:

$$b_1 = \frac{d_eM^2h_1}{f(1+M) - Mh_1} \simeq \frac{d_eM^2}{f(1+M)}h_1 \tag{10}$$

Repeating the procedure for different distances, h_2, h_3,…, a set of image separations, b_2, b_3,…, can be measured. Equation (10) suggests that the relation between the separation b and distance h should be approximated by a straight line. Using a least square curve fit, the slope of the line can be found and d_e can be determined given the focus length of the lens, f, and the magnification, M. The focus length f is a known parameter of the lens, and the magnification M is obtained by directly measuring an exact known length in physical space in the image. In this way, the system of equations used to describe DDPIV systems with a single-element lens can be used to describe DDPIV systems with a multi-element lens, thereby allowing for its methodology to determine 3D velocities.

5.2 Multi-surface refraction correction

In practice, light passes through the fluid, the transparent container wall, and the air before entering the lens system. As shown in Fig. 10, the multiple refractions will change the path of the incident ray and make the measured Z location appear smaller than its actual location, Z', for the case without fluid in the test section. For the case with fluid in the test section, the fluid index of

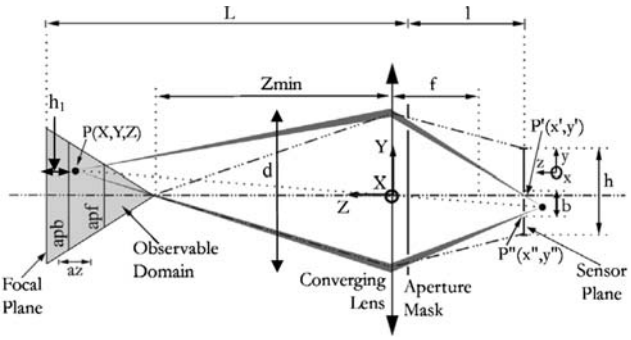

Fig. 9 Two-dimensional projection of the 3D defocusing model (Kajitani and Dabiri 2005)

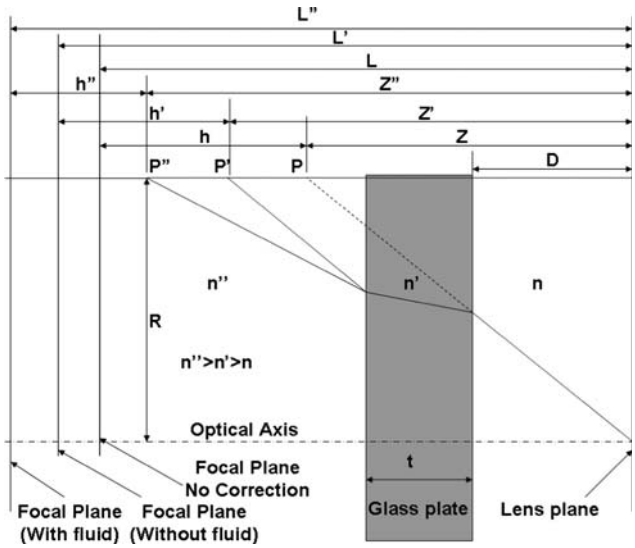

Fig. 10 Parameters associated with correcting for multi-surface refractions (adapted from Pereira and Gharib 2002)

refraction is different from that of the glass plate, thus resulting in an actual location Z'', different than Z'. Z'' is usually larger than Z', because the fluid index of refraction (water, $n'' = 1.333$) is smaller than the glass plate's index of refraction ($n' = 1.5$). The correction for the Z location due to such refractions is derived in Pereira and Gharib (2002) as follow:

$$Z'' = D + t + \left[Z - D - \frac{t}{\Omega(n')}\right] \times \Omega(n'')$$
$$\text{with } \Omega(v) = \sqrt{\frac{R^2}{Z^2}\left[\left(\frac{v}{n}\right)^2 - 1\right] + \left(\frac{v}{n}\right)^2} \simeq \sqrt{\left(\frac{v}{n}\right)^2} = \frac{v}{n},$$
$$\text{for } R = X^2 + Y^2 \text{ and } R \ll Z \tag{11}$$

where D is the distance from the lens plane to the bottom surface of the test section, t is the thickness of the bottom surface of the test section, and n, n' and n'' are the indices of refraction of air, glass and fluid, respectively. The simplification shown in Eq. (11) is valid since in the present configuration $R < 5$ mm and $Z > 140$ mm. Since the actual Z location is now Z'', the depth, h, used in Sect. 5.1 needs to be adjusted due to refractive effects through multiple surfaces to obtain a more accurate d_e. For the case without fluid, the actual particle location Z', is calculated using the same Eq. (11), with $n'' = 1$, indicating the fluid is air.

To correct for d_e, L from Eq. (8) is substituted in Eq. (6), resulting in

$$Z = \frac{f^2(1+M)d_e}{bf + dMf}. \tag{12}$$

In Eq. (7), L and Z are replaced by their effective values, L'' and Z'', respectively, where $L = Z|_{b=0}$. h is also be replaced by its effective value, h''

$$h'' = \frac{h}{\Omega(n'')} = L - Z, \tag{13}$$

resulting in the corrected effective d'_e, d''_e,

$$d''_e = \frac{b_1}{M}\left(\frac{f(1+M)}{Mh''} - 1\right). \tag{14}$$

Similarly, assuming $f \gg h_1$, the relation of b_1 and h_1 can be written as:

$$b_1 = \frac{d''_e M^2 h''_1}{f(1+M) - Mh''_1} \simeq \frac{d''_e M^2}{f(1+M)} h''_1. \tag{15}$$

Equation (15) is similar to Eq. (10); however, the effective d_e is replaced by d''_e, which has a refraction correction effect due to the index refraction of the fluid, n''. It is interesting that Eq. (15) shows that d''_e is not affected by the glass plate's index of refraction, and that the depth of the fluid does not affect Z'' or d''_e.

The increase in the length of the effective pinhole separation and the multi-surface refraction correction, also affect the sensitivity of the system. For a system without fluid, Willert and Gharib (1992) defined this sensitivity as the change of the triplet image size to the change of depth

$$\frac{\partial b}{\partial Z} = -\frac{Md_eL}{Z^2}, \tag{16}$$

where

$$Z = \left(\frac{1}{L} + \frac{b}{Md_eL}\right). \tag{17}$$

Using d''_e instead of d_e in Eq. (6), and using it to replace Z in Eq. (11), it can be shown that with multi-surface refraction corrections, the system sensitivity is

$$\frac{\partial b}{\partial Z''} = -\frac{Md''_eL}{Z''^2}\frac{n}{n''}. \tag{18}$$

It can be immediately seen that an increased effective pinhole separation increases the system sensitivity, while the index of refraction ratio will most often decrease the sensitivity, since in most applications, n corresponds to the refraction index of air, while n'' corresponds to the refraction index of the fluid.

5.3 Image processing

Images are captured by a frame grabber into a computer, and processed by a 4-stage image processing procedure to calculate the particle locations, as shown in Fig. 11. Upon particle identification, triplets and velocities are determined via procedures that have been previously published (Gharib et al. 1998; Pereira et al. 2000). In the first stage, the raw image is pre-processed to eliminate the background variation. The procedure is comprised of contrast enhancement and a Gaussian band-pass filter to reduce the high-frequency signal noise and the low-frequency bulk color variation of the background. The second stage separates the particle images within the triplets by separating the *CMY* colors. The third stage post-processes the images, where the background of each grayscale image is removed by thresholding. In the final stage, these particle images are analyzed to identify triplets, then particles locations in spatial coordinates, and finally the velocity field (Gharib et al. 1998; Pereira et al. 2000).

5.4 Calibration results

Figure 12 shows the calibration results for the image separation, b, versus the depth, h, for the cases with and without fluid present in the test section, where the linear fit equation is forced through the origin, since the separation

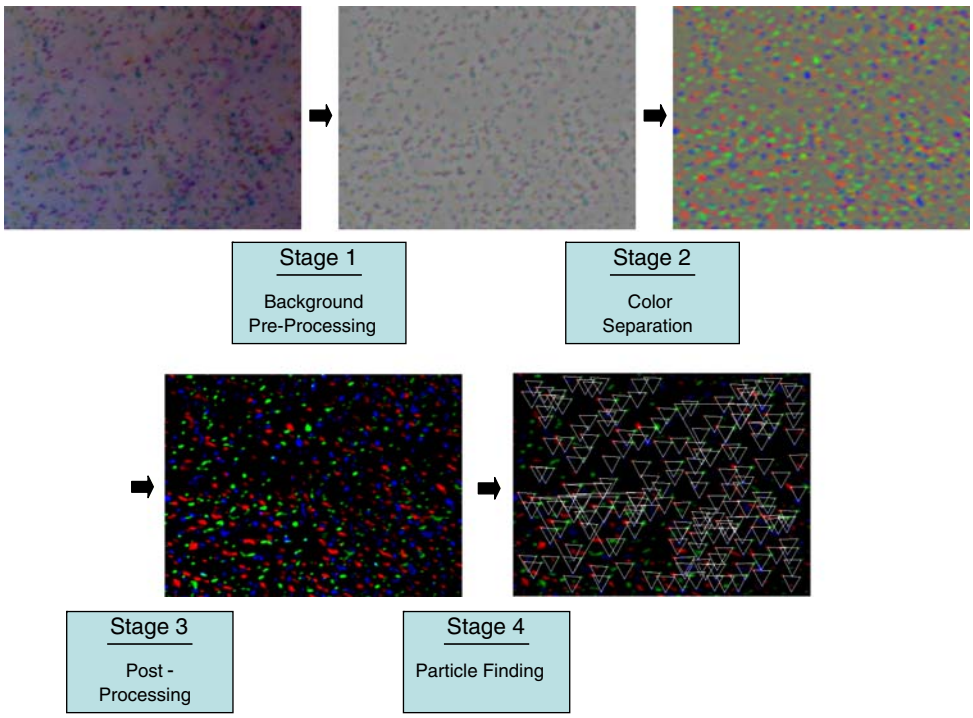

Fig. 11 The four-stage process for finding volumetric velocity fields

distance, b, must be zero when the depth, h, is zero. This equation is $b = 34.58\ h$, with a correlation coefficient of 0.9998. The high correlation coefficient to the linear fit indicates that the approximations made in Eqs. (10) and (15) are accurate and that the effective separation, d'_e, can be accurately extracted from the slope. Using Eq. (10) and the slope of the linear fit, d'_e is found to be 25.47 mm, which is then used to determine the Z' location of the particles in the flow field using Eqs. (6) and (11). In an alternative approach, the variation of the calculated d'_e values are plotted against the depth, h, as shown in Fig. 13. The averaged value of $d'_{e\,(avg)}$ using this approach is 25.31 mm, shown by the straight line in Fig. 13. Both approaches therefore provide nearly identical results, as the former is within 0.6% of the latter. The corresponding effective radial distance from the optical axis to the pinhole center γ'_e, using these two approaches is 14.71 mm and 14.61 mm, respectively.

Figure 12 also shows the resulting particle image separation versus depth with fluid in the test section, which is clearly different than the case without fluid in the test section. In re-performing the calibration procedure outlined in Sect. 5.1 and 5.2, the test section is filled with water ($n'' = 1.333$), allowing the heavier particles to stay on the bottom surface of the test section. The linear fit equation is forced through the origin resulting in $b = 39.15\ h$, with a correlation coefficient of 0.99985. Interestingly, the linear fit without forcing the curve through the origin is $b = 39.10\ h + 0.05719$, with a correlation coefficient of $R = 0.99985$. This further suggests that since the

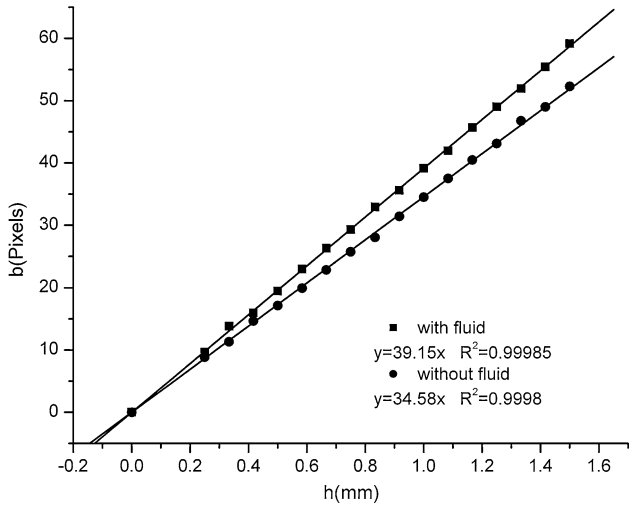

Fig. 12 Particle image separation, b, versus depth, h. The shown curve fits are forced through zero

y-intercept of this equation, which is the biased separation distance, b, in pixel, is nearly zero, that the procedure for determining an effective d_e is accurate and valid. Extracting d''_e from the slope of the calibration curve shown in Fig. 12 results in a value of 38.46 mm. Averaging the $d''_{e\,(avg)}$ values for different depth locations (see Fig. 13) results in a value of 38.27 mm, which is within 0.1% of the former value. The corresponding radial distance from the optical axis to the pinhole center, γ''_e, is 22.20 and 22.09 mm, respectively.

Regarding the sensitivity of the system (see Eq. (18)), the larger pinhole separation increases the sensitivity by a

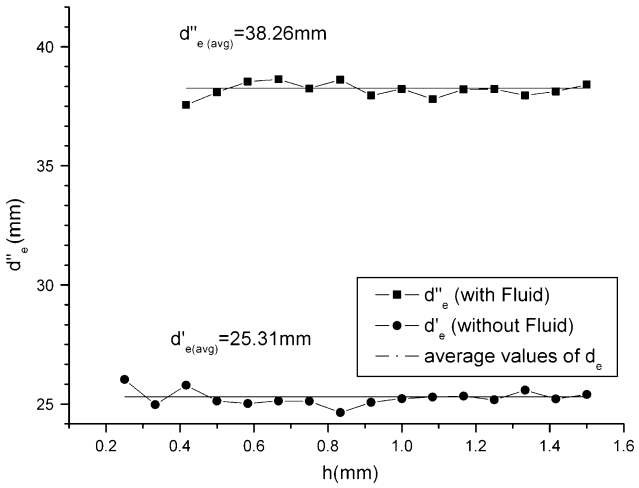

Fig. 13 Variation of effective d' versus depth h

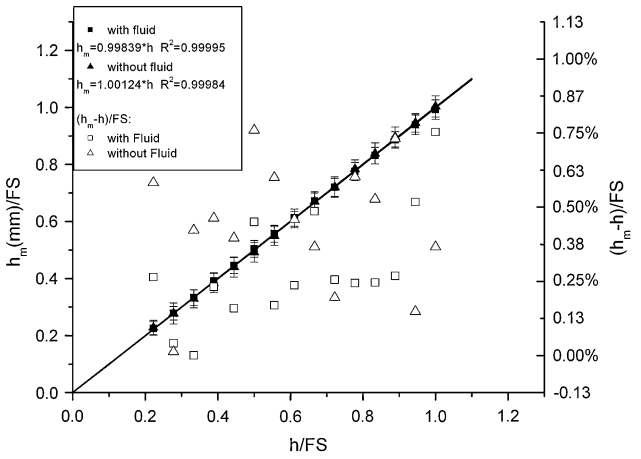

Fig. 14 Measured displacement, h_m, versus true displacement, h, and relative error with respect to the full depth range. The shown curve fits are forced through zero. The *open symbols* correspond to the right axis, while the *closed symbols* correspond to the left axis

factor of 2.55, while the refractive index ratio decreases the sensitivity by a factor of 1.333, resulting in a total increase in system sensitivity by a factor of 1.91.

6 Uncertainty analysis

To measure the uncertainty of the modified DDPIV system using the correction for multi-surface refractions, the test section is used with the polystyrene particles randomly distributed on the surface of the bottom plate. Starting from the focus plane, the test section is moved towards the camera to perform the calibration test discussed in the previous section. Images are taken at known depths, h, (determined by using a translation stage) until the triplet images are not detectable. Then images at each Z location are processed, upon which their (x, y) locations are compared to their focal plane locations, and their Z locations are compared with their actual Z locations. Thus the in-plane and out-of-plane RMS error can be calculated for each location.

Figure 14 shows the measured relative Z-axis displacement, h_m, versus the true displacement, h. The depth range, FS, used for the normalization is 1.5 mm. The cases with and without fluid clearly show that the suggested procedure, which uses an effective d_e incorporating the multi-surface refraction correction, accurately calculates the depth locations of the particles, as the linear curve fit is almost the identity line, with very high correlation coefficients. Interestingly, the linear curve fits without forcing the curve through the origin are $b = 0.98968\ h + 0.00614$ with $R = 0.99995$ for the case with fluid, and $b = 1.009\ h - 0.0056$ with $R = 0.99984$ for the case without fluid. Since the y-intercepts are nearly zero, these results clearly show that there is no inherent offset bias in the determination of the depth location. Furthermore, the relative error, $(h_m - h)/FS$, of the observable Z-axis displacements of the system is within 1% for cases with and without fluid, indicating that the depth location calculations are highly accurate.

The results of the in-plane and out-of-plane errors, shown in Fig. 15, are also normalized by FS. For the cases with and without fluid, the out-of-plane (Z) RMS errors are about 0.019 and 0.022 (0.0285 and 0.033 mm), respectively, and the in-plane (X, Y) RMS errors are about 0.003 and 0.002 (0.0045 and 0.003 mm), respectively. These errors are within 2.5% of the full depth range in the out-of-plane direction and 0.4% in the in-plane direction. In comparison for cases with fluid, Pereira et al. (2007) report values of 0.0045 and 0.011, and Yoon and Kim (2006) report values of 0.0011 and 0.003 for in-plane and out-of-plane normalized errors, respectively. As pointed out by Pereira (2007), the larger out-of-plane to in-plane error ratio of the present system is a consequence of the larger focal distance ($L = 145$ mm) with respect to the effective pinhole separation, d_e'' (38.26 mm).

Figure 16 shows the error ratio, the out-of-plane error $\delta(\mathrm{d}Z)$ to the in-plane error $\delta(\mathrm{d}X)$ and $\delta(dY)$, respectively, compared with the theoretical values derived by Kajitani and Dabiri (2005), which used geometric uncertainty analysis,

$$\varepsilon_X = \frac{\delta(\mathrm{d}Z)}{\delta(\mathrm{d}X)} = \frac{\sqrt{3}|Z|}{d\sqrt{1+\frac{3X^2}{d_e^2}}}, \qquad \varepsilon_Y = \frac{\delta(\mathrm{d}Z)}{\delta(\mathrm{d}Y)} = \frac{\sqrt{3}|Z|}{d\sqrt{1+\frac{3Y^2}{d_e^2}}}. \tag{19}$$

The theoretical values for the case with and without fluid are 6.59 and 9.91, respectively. The experimental averaged values of ε_X and ε_Y are 6.19 and 6.02, respectively, for the case with fluid, and 10.84 and 11.07, respectively, for the

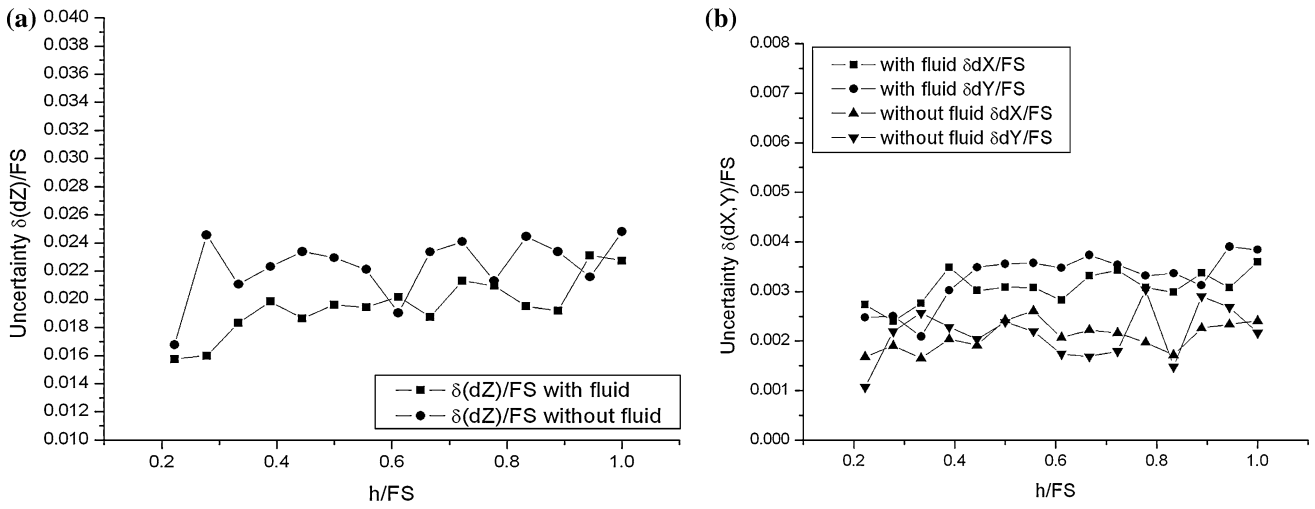

Fig. 15 **a** Out-of-plane (*Z*) and **b** in-plane (*XY*) RMS errors

case without fluid. The result is slightly smaller than the theoretical value for the case with fluid and larger for the case without fluid. As such, the theoretical values, which are only based on geometric uncertainty analyses, are within 10.5% of the experimental values, suggesting that this calibration approach is well-founded.

7 Practical implementation

To demonstrate the feasibility of this system, an experiment is performed, where the test section is filled with a 30% glycerol–water solution, and is densely seeded with polystyrene particles. The top and bottom of the test section are heated to 60 and 80°C, respectively, thereby generating buoyancy-driven flow. The imaged volume is 3.35 × 2.5 × 1.5 mm. Figure 17 shows the comparison of the original image, the pre-processed image, the resulting image after color separation, and the image showing identified triplets. Comparison of Fig. 17a, b shows the improvement due to preprocessing the background. The effect of the color separation algorithm is shown by comparing Fig. 17b and c, where the cyan, yellow and magenta colors are converted to pure (intensity value of 255) red, green, and blue colors. The identified triplets are shown in Fig. 17d, where the number of particles found in the frame shown is 347 particles.

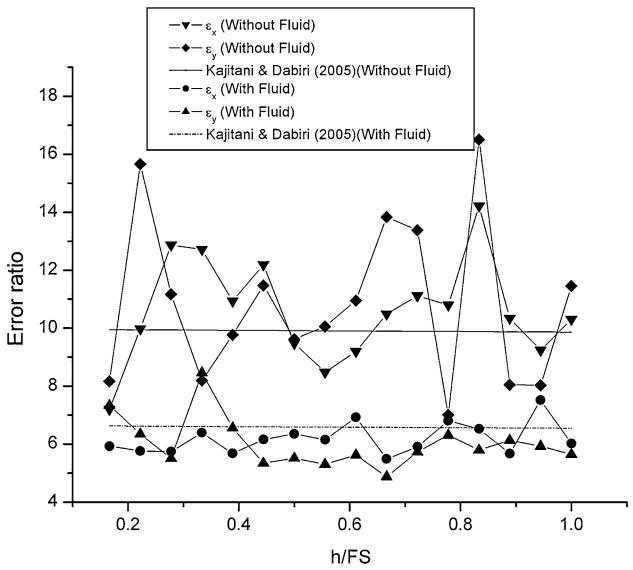

Fig. 16 Out-of-plane to in-plane error ratio compared with theoretical values

The velocity field is obtained by processing two successive particle fields, as detailed in Pereira et al. (2000). Figure 18a shows the particle pairs from two successive image frames and Fig. 18b is the resulting instantaneous velocity field. The velocity field is generated with an interrogation voxel (volume element) size of 1.2 mm × 0.9 mm × 0.9 mm, and voxel spacings of 0.6 mm × 0.45 mm × 0.45 mm, respectively. This setting provides 50% overlap of adjacent voxels, thereby generating 343 vectors in the field.

8 Conclusion

A color-coded backlighted single camera DDPIV system is developed to overcome the difficulties of the original single camera system. A pinhole mask with three color filtered pinholes is used to color-code each exposure of the defocused particle image, and a color splitting algorithm is developed to solve the particle identification problem. To overcome the limiting need for high intensity illumination for DDPIV systems, the modified system uses backlighting

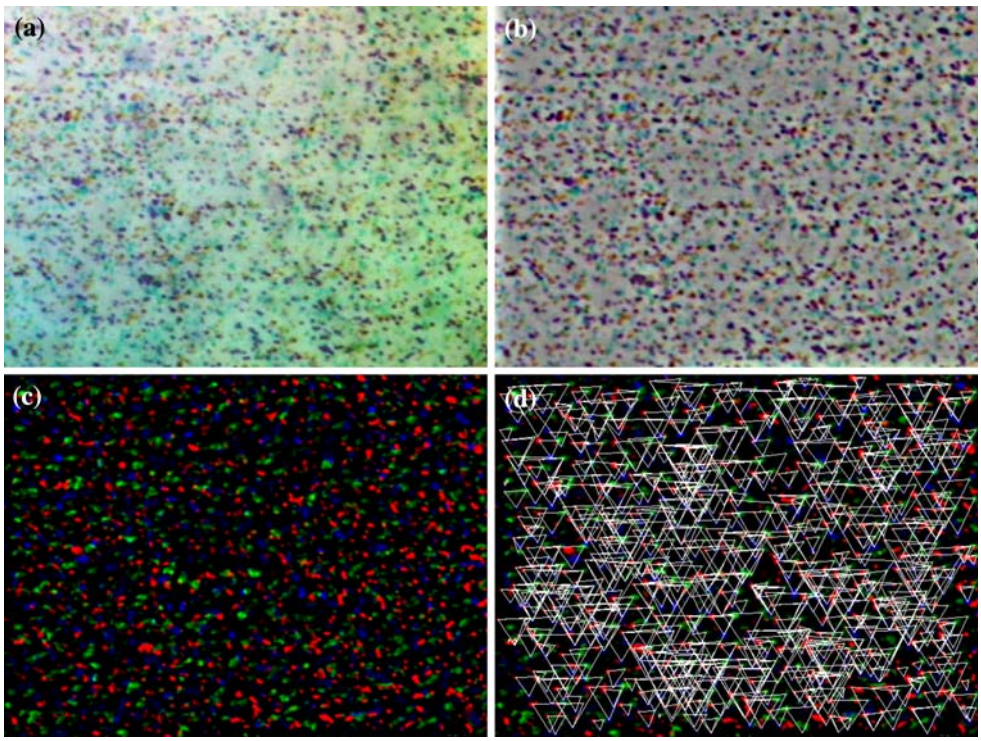

Fig. 17 **a** Original image **b** pre-processed image **c** color separation **d** triplets found by DDPIV software

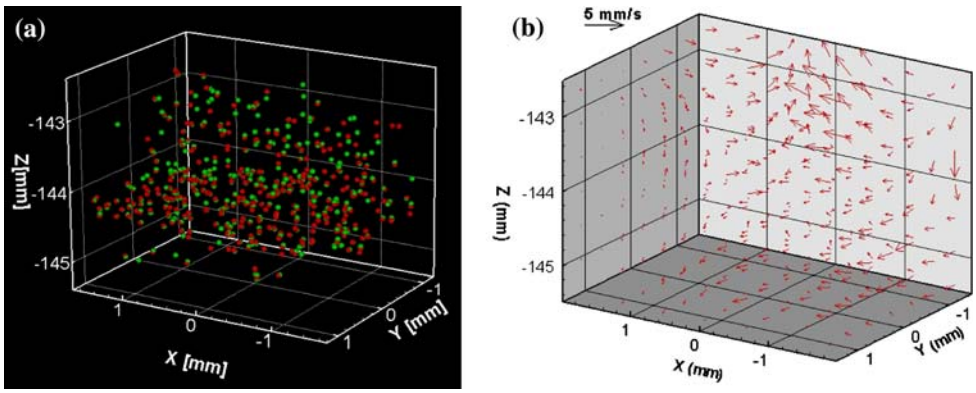

Fig. 18 **a** particle pair image **b** 3-D flow field found by DDPIV routines. The particles found in the first and second frames are shown in *red and green*, respectively

in conjunction with black particles. A calibration procedure to find the effective pinhole spacing, d_e, was developed to give more accurate particle spatial coordinates, and a correction to the effective pinhole spacing, d_e'', for multi-surface refractions is also developed and validated by experiments. The uncertainty of the measured particle location is within 1.5% of the full depth range in the out-of-plane direction and 0.15% of the in-plane direction. The imaged volume of the system is $3.35 \times 2.5 \times 1.5$ mm. This technique is applied to a buoyancy-driven flow and a 3D velocity field is successfully extracted and shown.

While the color-coded backlighted single camera DDPIV system developed here has been demonstrated to be suitable for visualizing and quantifying micro-scale fluid flows, the use of backlighting, in conjunction with non-reflective particles can also be used to significantly reduce the illumination power requirements for multiple-CCD DDPIV systems. Furthermore, for imaging higher speed flows, rather than using a single pulsed white light source, two pulsed white light sources can be used to asynchronously illuminate the flow, analogous to the dual Nd:YAG illumination systems used in DPIV systems.

Acknowledgments We would like to thank professor Gamal Khalil from the UW Chemistry department for his help in dying the polystyrene particles. This work is supported by the National Institute of Health (SRS 20309/SAP 1004717).

References

Estevadeordal J, Goss L (2005) PIV with LED: particle shadow velocimetry (PSV), 43rd AIAA Aerospace Sciences Meeting and Exhibit, January 10–13, Reno, Nevada

Gharib M, Modarress D, Dabiri D, Pereira F, Taugwalder F (1998) Development and application of a defocusing three dimensional DPIV technique for the mapping of two-phase bubbly flows. In: Processings of 9th international symposium on applications of laser techniques to fluid mechanics. Instituto Superior Técnico, Lisbon, Portugal, 16.5.1–16.5.7

Kajitani L, Dabiri D (2005) A full three-dimensional characterization of defocusing digital particle image velocimetry. Meas Sci Technol 16:790–804

Pereira F, Gharib M (2002) Defocusing digital particle image velocimetry and the three-dimensional characterization of two-phase flows. Meas Sci Technol 13:683–694

Pereira F, Gharib M, Dabiri D, Modarress D (2000) Defocusing digital particle image velocimetry. A 3-component 3-dimensional DPIV measurement technique. Application to bubbly flows. Exp Fluids 29:S78-S84

Pereira F, Lu J, Castano-Graff E, Gharib M (2007) Microscale 3D flow mapping with μ DDPIV. Exp Fluids 42:589–599

Pratt WK (1991) Digital image processing. Wiley, New York

Willert CE, Gharib M (1992) Three-dimensional particle imaging with a single camera. Exp Fluids 12:353–358

Yoon SY, Kim KC (2006) 3D particle position and 3D velocity field measurement in a microvolume via the defocusing concept. Meas Sci Technol 17:2897–2905